Physics of Fluids

RESEARCH ARTICLE | APRIL 04 2023

Numerical study of periodic flame flashback in a cavity-based scramjet combustor

Shengzu Guo ; Xu Zhang ; Qili Liu ; Lianjie Yue

Physics of Fluids 35, 045108 (2023)
https://doi.org/10.1063/5.0142210

Physics of Fluids ARTICLE scitation.org/journal/phf

Numerical study of periodic flame flashback in a cavity-based scramjet combustor

Cite as: Phys. Fluids **35**, 045108 (2023); doi: 10.1063/5.0142210
Submitted: 12 January 2023 · Accepted: 15 March 2023 ·
Published Online: 4 April 2023

Shengzu Guo,[1,2] Xu Zhang,[1,a)] Qili Liu,[1,2] and Lianjie Yue[1,2,a)]

AFFILIATIONS

[1]State Key Laboratory of High Temperature Gas Dynamics, Institute of Mechanics, Chinese Academy of Sciences, Beijing 100190, China
[2]School of Engineering Science, University of Chinese Academy of Sciences, Beijing 100049, China

[a)]**Authors to whom correspondence should be addressed:** zhangxu@imech.ac.cn and yuelj@imech.ac.cn

ABSTRACT

The periodic flame flashback phenomenon in an ethylene-fueled cavity-based scramjet combustor was numerically investigated by a three-dimensional unsteady Reynolds-averaged Navier–Stokes solver with two-step kinetics. The air inflow stagnation temperature is 1225 K, and its Mach number is 2.6. Spectral analyses revealed the combustion oscillations with flame flashbacks maintained in the separated scramjet mode with the establishment/vanishment of flow separation near the fuel injector, differing from previous studies of flame flashbacks connected to the ramjet/scramjet mode transitions. A mechanism with four evolution stages was proposed to elucidate the flow-flame interaction. In stage I, a rapid flame flashback upstream and shock-train extension were caused by the high-temperature induced auto-ignition tendency of well-mixed unburned gas in the near-sidewall low-speed region. In stage II, the combustion-induced back pressure and shock train gradually achieved an aerodynamic balance. The combustion flow barely changed in stage III. Meanwhile, a simplified model suggested that the gradual temperature rises occurring upstream of the cavity and away from the sidewall were caused by spanwise heat conduction. The higher temperatures would cause upstream flame propagation with enhanced heat release due to auto-ignition. However, the enhanced heat release occurred mostly in the subsonic flow, resulting in pressure decreases according to one-dimensional flow equations. A smaller near-sidewall separation was produced by the lower back-pressures, which prompted the rapid flame recession downstream in stage IV. Moreover, a simplified flame-spreading model was proposed to illuminate the flame propagation nature. The comparison of flame speeds with theoretical estimations indicated that the current flame was in the regime of turbulent flame propagation, rather than the C–J detonation or deflagration speculated in previous studies.

NOMENCLATURE

HRR	Heat release rate
ER	Equivalence ratio
F_t	Combustor thrust
Ma	Mach number
p	Pressure
T	Temperature
t	Time
URANS	Unsteady Reynolds-averaged Navier–Stokes
X	Mole fraction of certain combustible species
x, y, z	The three coordinates of a Cartesian coordinate system
W	Combustor width
τ_{res}	Fuel residence time
τ_{ign}	Ignition delay time

Subscripts/Superscripts

c	Wall-pressure monitoring point at the cavity bottom
i	Wall-pressure monitoring point near the injector
in	The combustor inflow
L	Local value at certain spatial point
min	The minimum value
ref	The reference value
T	The total value of the combustor
$*$	The stagnation flow parameter

I. INTRODUCTION

The scramjet engine is a promising hypersonic air-breathing propulsion system.[1] A scramjet combustor typically contains a constant-area isolator and an expansive combustion duct. As combustor inflows

are supersonic, flame-holding devices are used to stabilize flames, such as air throttling,[2–4] hot pilot gas,[4–6] ramps,[7] cavities,[8–12] and struts.[13–15] The cavities are favored because of low pressure losses in the lower hypersonic flight envelope. Combustions are generally unsteady with flow and flame oscillations[8,15,16] in the scramjet combustors. Thermo-acoustic instabilities are common factors driving combustion oscillations.[17–20] The instabilities exist in the subsonic regions of combustor mainflows and the flameholders' low-speed regions. The former had been detailly elucidated in our previous study.[20] Recently, another type of combustion oscillation phenomenon, i.e., the periodic flame flashback, was observed by some researchers.[21–33] The flame flashbacks generally showed as sudden upstream flame propagations with proliferated flame intensities. The dominant frequencies of a few tens or hundreds Hz were generally lower than those of thermo-acoustic oscillations. Moreover, the periodic flame flashbacks could cause large-amplitude oscillations of thrusts, which are adverse for smooth engine control. Therefore, stable scramjet engine operations require a thorough understanding of the periodic flame flashback phenomenon and the mechanism.

Scramjet engines can operate in different combustion modes.[34–36] Traditional dual-mode means that a combustor can operate in dual types of combustion states, including the ramjet (subsonic combustion) mode and the scramjet (supersonic combustion) mode. They can be distinguished by the minimum Mach number $Ma_{\min}$, assuming one-dimensional (1D) flows.[34] A combustor is in the ramjet mode if $Ma_{\min} < 1.0$; otherwise, it is in the scramjet mode. The scramjet mode is further subdivided into the separated scramjet mode with a pre-combustion shock-train and flow separation and the shock-free scramjet mode without shock-induced separation. Based on two-dimensional (2D) flame distributions, recent researchers could classify different flame stabilization modes.[21,37] The jet-wake stabilized mode and the cavity stabilized mode are generally observed in cavity-based combustors with upstream fuel injections.[21] The difference is that the flame fronts are upstream and downstream of the cavity fore-walls, respectively. The cavity stabilized mode is subdivided into the combined cavity shear-layer/recirculation stabilized mode and the cavity shear-layer stabilized mode.[37] The combined mode has distinct flames in the cavity's recirculation region, while the latter mode does not.

The periodic flame flashback phenomena in cavity-based combustors had been widely investigated.[21–29] Micka *et al.*[21] first observed these phenomena behaving as flame oscillations between the jet-wake stabilized mode and the cavity stabilized mode with a set of dominant frequencies between 5 and 20 Hz. They speculated these to be related to fluid dynamic, acoustic, or facility-dependent fluctuations. Fotia *et al.*[22] further dissected the mechanism being dominated by the self-sustaining cavity shear-layer instability. Sun *et al.*[23–29] likewise observed the flame flashback oscillations with dominant frequencies around 10–300 Hz. The experimental flashback speeds were between the theoretical Chapman–Jouguet (C–J) detonation and deflagration speeds.[23,24] Thus, the flame flashback was considered likely an accelerated flame propagation with a deflagration-to-detonation transition. Zhao *et al.*[26–29] found that the flame flashback could be triggered by the thermal choking formed by strong interactions between the combustion and the flow separations downstream of the cavities. Cao *et al.*[30] numerically revealed that the jet-wake flame flashback was driven by the backpressure-induced flow separations. Flame flashbacks in strut-based combustors were also observed by Zhu *et al.*,[31,32] which were believed to be likely accompanied by detonation waves. In addition, the generation of recirculation and low-speed regions in boundary layers was considered to induce the strut-based flashback.[33] In short, previous studies offered fundamental understandings of the periodic flame flashbacks and suggested inconsistent explanations. However, an in-depth explanation of the flame flow evolution had not been completed, and the flame propagation mechanism remained controversial.

The current study numerically investigated the flame flashback phenomenon in a cavity-based scramjet combustor. Ethylene fuel was injected transversely upstream of the cavity. This paper is organized as follows: Sec. II introduces the combustor configuration, numerical details, experimental validation, and grid convergence verification. Results illustrate a periodic combustion oscillation process with the flame flashback. Section III A dissects the overall characteristics of this process. Section III B elucidates its evolution mechanism by analyses of flame flow structures. Then, Sec. III C identifies the flame propagation mechanism through flame speed comparisons to theoretical estimations.

II. MATERIALS AND METHODS

A. Combustor configuration and inflow conditions

Figure 1 shows a 2D schematic diagram of the combustor model, which was symmetric in both the lateral and spanwise directions. The combustor contained a 400 mm long constant-area isolator and a 581 mm long 3.6° expansive duct with cavities. The model width W was constantly 80 mm, and the inlet height was 40 mm. The cavity was located 100 mm downstream of the isolator exit and spanned the combustor width. It has a depth of 17 mm, a length of 65 mm, and a 24° ramp angle. A Cartesian coordinate system was established with the origin at the center of the isolator inlet. The x, y, z coordinates were along the streamwise, lateral, and spanwise directions, respectively. Ethylene fuel was injected 40 mm downstream of the isolator exit. The injector included an array of five wall-normal sonic orifices of diameter 1.5 mm on the upper and lower walls, respectively. The three orifices with non-negative z coordinates were located at $z/W = 0$, 3/16, and 3/8, respectively. Two monitoring points with the wall-pressures marked as "p_c" and "p_i" were located at the cavity bottom and near the injector, respectively.

Table I lists the isolator inflow parameters, simulating a flight Mach number of 5.0 at an altitude of 21.3 km. The inflow air contained 21% oxygen and 79% nitrogen in mole fractions. The inflow Mach number Ma_{in}, stagnation temperature T^*_{in}, and stagnation pressure p^*_{in} were 2.6, 1225 K, and 1836 kPa, respectively. The inflow static temperature T_{in} was 555 K. The reference pressure p_{ref} for normalizations was equal to the inflow static pressure p_{in} of 86 kPa. Ethylene fuel was injected at the temperature of 300 K, and the total equivalence ratio (ER_T) was 0.29.

B. Numerical method

This study utilized the three-dimensional (3D) unsteady Reynolds-averaged Navier–Stokes (URANS) solver to simulate the supersonic turbulent reactive flows, similar to our former numerical study.[20] The finite volume method and the pressure-based SIMPLE-type algorithm were applied to solve the 3D single-phase, multi-species URANS equations, including the continuity and momentum equations, and additional scalar transport equations of turbulent quantities,

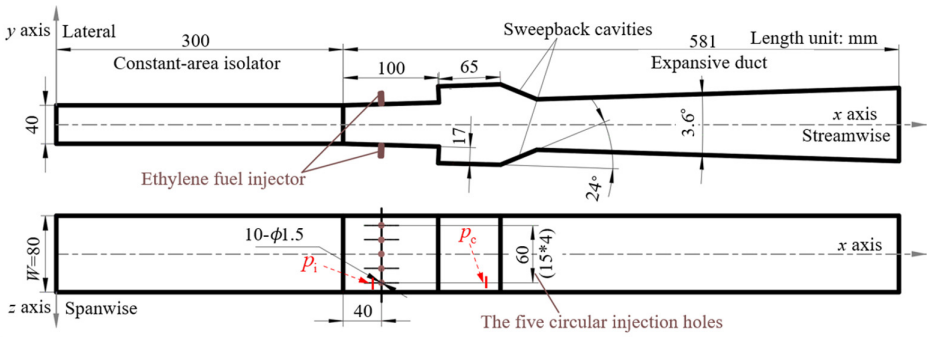

FIG. 1. Schematic diagram of the combustor.

energy, and species. Density and convection terms were discretized by the second-order upwind schemes. Pressure and diffusion terms were discretized by the second-order central differencing schemes. Temporal discretization was performed by the second-order backward Euler implicit scheme. The cell center gradients were computed by the least squares cell-based method. The minmod slope-limiter was utilized for the total-variation-diminishing (TVD) properties. Turbulence closure was achieved by the Menter's shear-stress transport (SST) k-ω model,[38] including viscous heating, compressible effects, and low-Reynolds-number corrections. The ethylene-air combustion species was taken as a mixture of ideal gases, and thermophysical mixture properties were calculated by the mass-weighted mixing law. The specific heat of each species was defined as a piecewise polynomial function of temperature from the NASA database that is valid up to 5000 K, and the thermal conductivity and viscosity were calculated by the kinetic theory. The validated two-step kinetic model ($C_2H_4 + 2O_2 \rightarrow 2CO + 2H_2O$, $CO + 0.5O_2 \rightleftarrows CO_2$) proposed by Westbrook *et al.*[39] was adopted for ethylene-air reactions. Turbulence/chemistry interactions were treated by the finite-rate/eddy-dissipation model. The time step size of 4×10^{-6} was carefully chosen for the time step independence, and the maximum sub-iteration number was 50.

C. Computational grid and boundary condition types

A multi-block hexahedron grid scheme was adopted for numerical accuracy. The computational grid contained a quarter of the combustor separated by symmetries. Wall-normal distance from each first-layer cell center was set to 0.001 mm for $y^+ < 1$. More than 20 layers of mesh were in the domain of $y^+ < 30$ to ensure calculation accuracies of turbulent boundary layers. Figure 2 presents the grid distribution near the cavity and the injector.

The inlets of the isolator and the injector were both designated as pressure inlet boundaries. The inlet turbulent intensities and viscosity ratios were specified as 1% and 1.0, respectively. The inlet boundary layers were ignored, and species mole fractions were specified. The isolator inflow was supersonic; hence, its stagnation temperature, stagnation pressure, and pressure were all specified as listed in Table I. As to the injector inlet, only the stagnation temperature and stagnation pressure needed to be specified because of sonic injection. The combustor outlet employed supersonic extrapolation. A mirror reflection was implemented on each symmetry. All walls were stationary, no-slip, and adiabatic.

TABLE I. The isolator inflow condition.

Ma_{in}	T^*_{in} (K)	p^*_{in} (kPa)	T_{in} (K)	p_{in} (kPa)
2.6	1225	1836	555	86

D. Experimental validation and grid convergence verification

The numerical method was validated by the comparison with previous experimental data of an ethylene-fueled scramjet combustor.[40] The experimental air inflow contained 21% O_2, 61% N_2, and 18% H_2O in mole fractions. The inflow Mach number, stagnation temperature, and stagnation pressure were 2.5, 1338 K, and 1520 kPa, respectively, similar to the parameters in Table I. The fuel ER_T was 0.22. Three computational grids, containing 210 $\times 10^6$ (coarse), 415 $\times 10^6$ (medium), and 686 $\times 10^6$ (fine) cells, respectively, were adopted to verify grid convergence. The medium grid had a similar resolution as the grid shown in Fig. 2. Figure 3 shows good agreement of normalized experimental and numerical wall-pressure distributions, which demonstrates the accuracy of the current numerical setup. Meanwhile, the medium-grid solution resembled the fine-grid solution more than the coarse-grid solution, proving that the medium grid possessed sufficient spatial resolution.

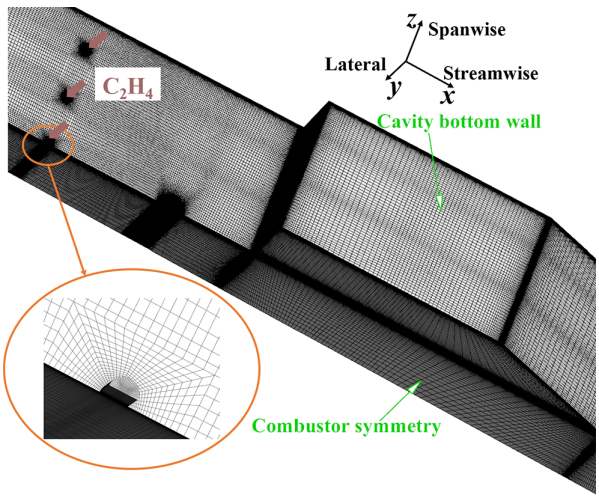

FIG. 2. Grid near the cavity and the injector.

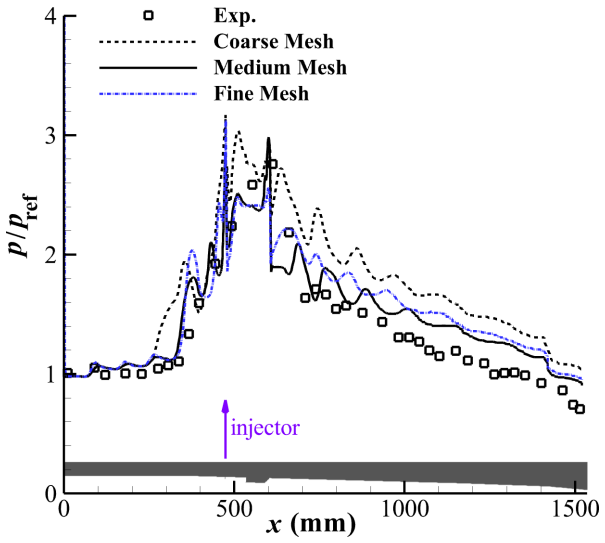

FIG. 3. Comparison of experimental and numerical wall-pressure distributions.

III. RESULTS AND DISCUSSION

A. Characteristics of the periodic flame flashback

This section will introduce the overall features of a periodic flame flashback phenomenon based on the current numerical results. As the heat release rate (HRR) represents flame intensity, Fig. 4 presents two typical states of 2D HRR translucency distributions with the most downstream and upstream flame fronts, respectively. The normalization reference value for HRR was 12 000 MW/m^3, close to the maximum flame intensity. This chart displays flame fronts upstream of the cavity in both states, indicating the flame maintained in the jet-wake stabilized mode during the whole periodic process. This was similar to our experimental observations,[41] while slightly differing from previous studies[21–29] of periodic flame flashbacks oscillating between the jet-wake stabilized mode and the cavity stabilized mode. Despite the little difference, the intrinsic mechanisms are similar and will be further discussed in Secs. III B and III C.

Thrust F_t was a concerned performance calculated by integration of the combustor wall-pressures and friction stresses. The wall-pressures p_c and p_i could be indicators of flame and shock-separation status. Figure 5 shows the time histories of F_t and the normalized wall-

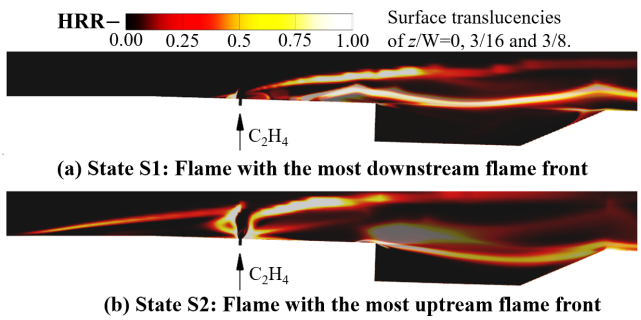

FIG. 4. Typical 2D flame translucencies during the periodic flame flashback.

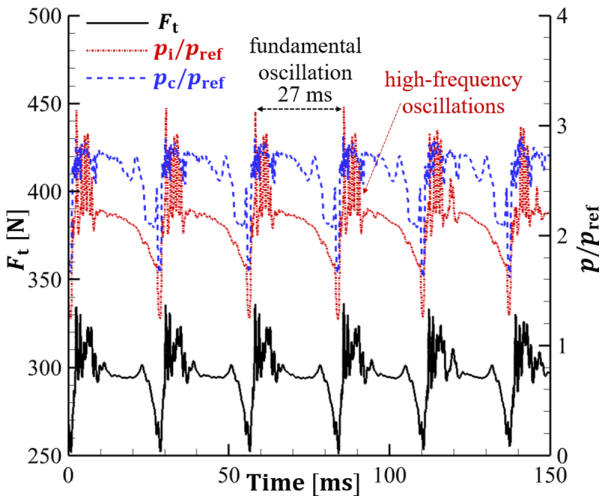

FIG. 5. Time history curves of F_t, p_i/p_{ref}, and p_c/p_{ref}.

pressures p_i/p_{ref} and p_c/p_{ref}. It can be seen that these parameters underwent a synchronous low-frequency oscillation with a fundamental period of about 27 ms. The variation percentage of a parameter during the fundamental period was defined as the difference value between the maximum and the minimum divided by the maximum value. The variation percentage of F_t, p_i/p_{ref}, and p_c/p_{ref} was as much as 25%, 60%, and 44%, respectively. F_t varied relatively smaller compared to p_i/p_{ref} and p_c/p_{ref} located near the injector and cavity. This indicated streamwise wall-pressure changes and relevant flame/shock-separation changes mainly occurred near the injector and cavity. In addition to the fundamental oscillation, other oscillations with much higher frequencies co-existed as shown in Fig. 5, and the variation percentages were much smaller. These differences indicated the driving mechanism of the fundamental oscillation differed from the high-frequency oscillations.

To further identify the difference between the fundamental and the high-frequency oscillations, spectral analyses are presented below. Figure 6 shows the amplitude-frequency characteristics of F_t, p_i/p_{ref}, and p_c/p_{ref} by FFT analyses. This chart illustrates two separate regions of dominant frequencies. The first region of 791–974 Hz was related to the high-frequency oscillations as shown in Fig. 5. These oscillations were inherently driven by thermo-acoustic instabilities in the subsonic regions of the mainflow as discussed in the previous study.[20] In the second region of 37–291 Hz, the dominant frequencies were close to integral multiples of the fundamental frequency of 37 Hz, which was consistent with the aforementioned fundamental period of about 27 ms. These oscillations were related to the periodic flame flashback process from observations. The frequency multiplication in these oscillations indicated that the process was probably attributed to certain feedback loops between the in-phase oscillating flame and flow fluctuations,[42] which was similar to the speculation of Micka *et al.*[21]

1D streamwise pressure distribution could provide basic features of combustion and flow separation status. Figure 7 presents the evolution contour of 1D streamwise pressure-rise p/p_{ref} distributions during a fundamental period. The p values were extracted from the centerline on the near-sidewall $z/W = 3/8$ surface for flow separation

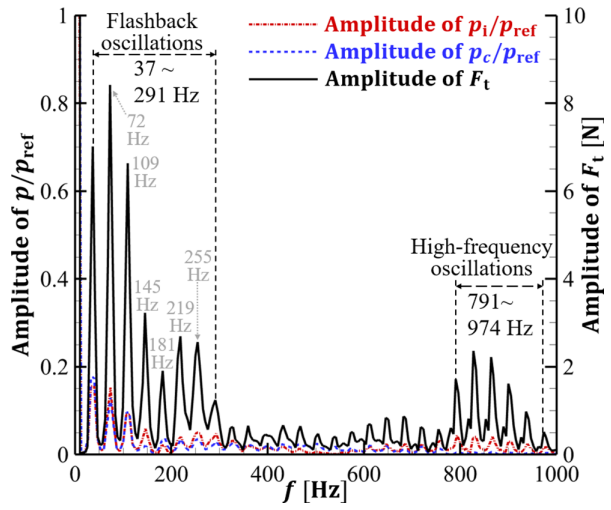

FIG. 6. Amplitude-frequency characteristic curves of F_t, p_i/p_{ref}, and p_c/p_{ref}.

monitoring as separation generally occurred near the sidewall. The process could be divided into I, II, III, and IV four stages based on the pressure-rise variation features, particularly the pressure-rise origin. In stage I, the pressure-rise origin abruptly moved upstream from about $x = 340$ mm near the injector to $x = 245$ mm, and the cavity pressure-rise p_c/p_{ref} largely increased from about 1.8 to 2.7. This indicated that the flow separation was established upstream of the injector with significantly enhanced combustion heat release. Practically, the flame flashback occurred in this stage, showing as the upstream flame propagation from states S1 to S2 in Fig. 4. Then, in stage II, the streamwise pressures underwent a transition from slight oscillations to a steady state, indicating the progressive establishment of aerodynamic balance in flame and flow interactions. In stage III, the streamwise pressures changed little temporarily. However, to some degree, the pressure-rise p_i/p_{ref} near the injector distinctly increased from about 2.8 to 3.2. This suggested that certain accumulated effects broke the aerodynamic balance. Then, in stage IV, the pressure-rise origin abruptly moved downstream back to about $x = 340$ mm with the p_c/p_{ref} decreasing back to 1.8, indicating the separation vanishment upstream of the injector and largely weakened heat release. Practically, the flame in this stage abruptly receded downstream from state S2 back to S1.

To recognize the ramjet/scramjet combustion mode during the periodic process, Fig. 8 plots the 1D mass-flux weighted average Mach number distributions of the representative states S1 and S2, respectively. The minimum pressure-rise p_m/p_{ref} needed for shock-induced separation was theoretically determined by the inflow, and it could be estimated as $p_m/p_{ref} = 1 + 0.5Ma_{in} = 2.3$.[35] Figure 8 shows that the maximum pressure-rises p_{max}/p_{ref} were larger than p_m/p_{ref} in both states, indicating flow separations. Thus, the combustion maintained in the separated scramjet mode during the entire process. This differed from previous studies[22–29] in which the flame flashbacks were speculated to be associated with ramjet/scramjet mode transitions with formations of thermal throats or thermal chokings. Meanwhile, the different pressure-rise origins indicated that this process was accompanied by the periodic establishment and vanishment of flow separation near the injector, identifying with Figs. 5 and 7.

B. Explanation of the flame flow evolution

Section III A has introduced the general characteristics of the periodic flame flashback phenomenon, which was suggestively accompanied by abrupt changes in flow separations and flame intensities. This section will further analyze the mechanism by explanations of flow and flame structural evolutions across the four stages from time $= t_1$ to t_7 divided in Fig. 7.

Stage I was a time duration with rapid upstream propagation of the flame front, namely, the flame flashback. Figure 9 presents the contours of temperature T and local equivalence ratio ER_L at the start of stage I. ER_L was calculated as below:

$$ER_L = \begin{cases} (3 \cdot X_{C_2H_4} + 0.5 \cdot X_{CO})/X_{O_2} & \text{if } X_{O_2} > X_{min}, \\ 0 & \text{if } X_{O_2} < X_{min}, \end{cases} \quad (1)$$

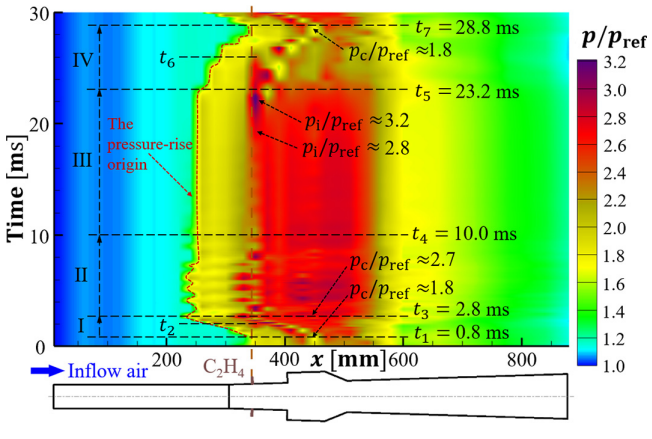

FIG. 7. Time history of streamwise pressure-rise distribution during the fundamental period.

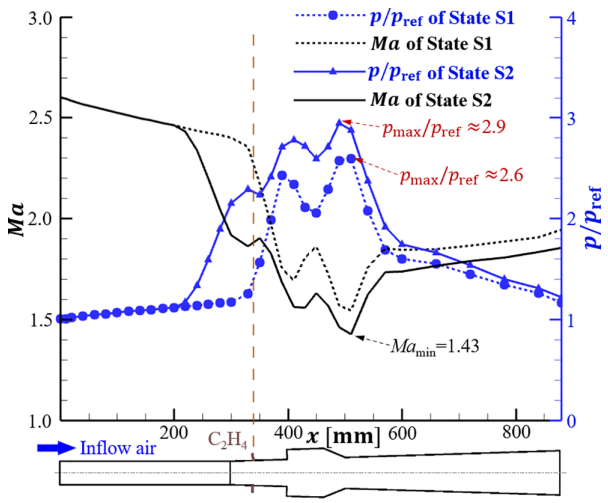

FIG. 8. Typical streamwise 1D averaged pressure and Mach number distributions.

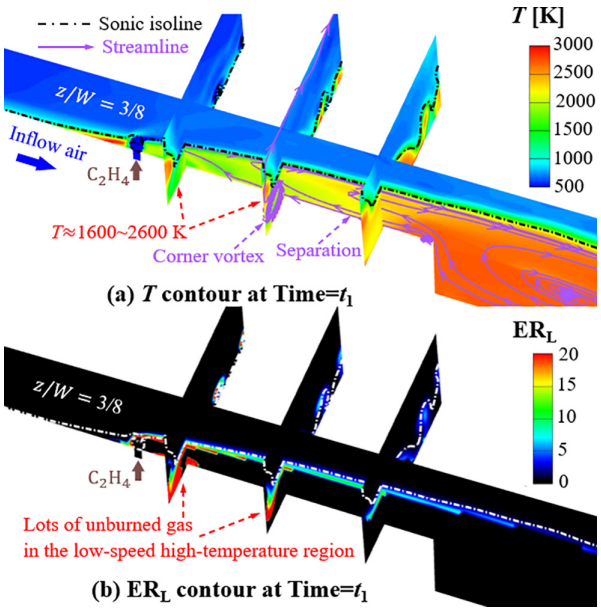

FIG. 9. The temperature T and local equivalence ratio ER_L contours at the start of stage I.

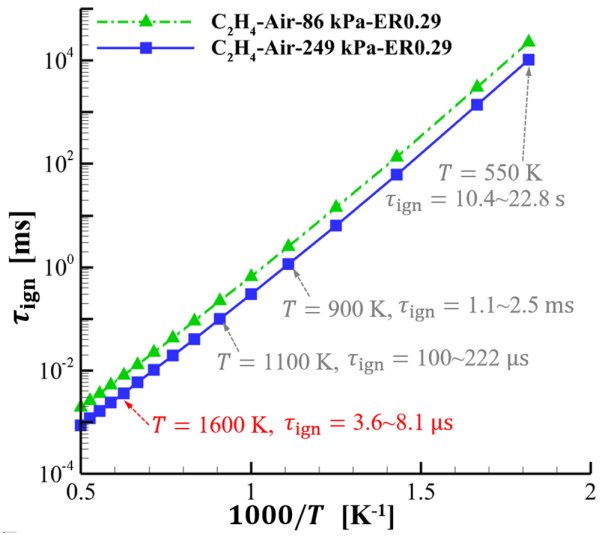

FIG. 10. Ignition delay time τ_{ign} vs 1000/T.

where $X_{C_2H_4}$, X_{CO}, and X_{O_2} were the mole fractions of combustible species C_2H_4, CO, and O_2 respectively. X_{min} was a threshold value set as 0.02 to exclude regions with negligible oxygen. Figure 9(a) illustrates that a large area of the low-speed high-temperature region was located near the sidewall with flow separation and corner vortexes, which could promote mixing and combustion. Meanwhile, Fig. 9(b) displays that much well-mixed unburnt gas existed in this region. Subsequent flame evolution could be speculated by estimations of fuel residence time τ_{res} and ignition delay time τ_{ign} as follows.

As the flames were commonly stabilized near the cavity, the distance from the injector to the cavity aft-wall was considered as the maximum mixing length $L = 0.161$ m. The inflow x-velocity u_x was about 1224 m/s. Thus, fuel residence time in the main flow was estimated as $\tau_{res-m} = L/u_x = 131\ \mu s$. The actual residence time in the near-sidewall high-temperature region would be longer because of lower flow speeds and separation. As shown in Fig. 8, the maximum pressure-rise p_{max}/p_{ref} across the periodic process was about 2.9 with the p_{max} of 249 kPa. Considering the inflow pressure of 86 kPa and the global ER_T of 0.29, Fig. 10 plots τ_{ign} of ethylene-air premixed gas vs $1000/T$ under the constant pressures by the aforementioned two-step kinetic model.[39] This chart demonstrated that in the near-sidewall low-speed region with temperatures higher than 1600 K, the τ_{ign} of lower than 8.1 μs was much less than the τ_{res-m} of 131 μs. Thus, the plentiful well-mixed unburnt gas in this region tended to be auto-ignited quickly.

Figure 11 presents the normalized HRR contours at time $= t_1$ and t_2, respectively. It could be seen that much flames abruptly propagated upstream of the injector with enhanced heat release, especially on the near-sidewall $z/W = 3/8$ surface. This was consistent with the above explanation referring to Figs. 9 and 10. According to 1D flow equations, the enhanced heat release contributed to an enlarged subsonic region[20] and higher back-pressures, which could drive the shock-train to become stronger and move upstream. The resultant shock reflection ahead of the injector could generate obvious separation as shown in Fig. 11(b), which in return would benefit mixing and combustion. Thus, the enhanced flame and flow separation ahead of the injector could persist for a relatively long time than stage I.

Figure 12 displays the normalized HRR contour at time $= t_3$, the end of stage I. It could be seen that the flame and flow separation kept existence ahead of the injector on the near-sidewall $z/W = 3/8$ surface. Meanwhile, by comparing Fig. 11(b), the flame and separation ahead of the cavity disappeared on the $z/W = 3/16$ surface away from the sidewall. The reason is explained below. Figure 13 presents the normalized pressure contour on the $z/W = 3/16$ surface at time $= t_2$ and t_3, respectively. This chart illustrated the upstream movement of the shock-train, which promoted near-sidewall separation and combustion as displayed in Fig. 12. Meanwhile, the normalized pressures p_{r1}/p_{ref} and p_{r2}/p_{ref} before and after the shock reflection downstream of the injector, respectively, became much closer, indicating shock weakening. The $z/W = 3/16$ surface was away from the sidewall, lacking sidewall boundary-layer and corner separation effect,[43] and thus, the flow was relatively difficult to be separated. Consequently, the weakened shock generated a reduced subsonic region, and the increased flow speeds were adverse for mixing and combustion. The subsequent flame recession in return could further reduce the subsonic region. As a result, the separation and flame disappeared ahead of the cavity on the $z/W = 3/16$ surface as shown in Fig. 12.

Stage II was a period in which the enhanced flame and the extended shock-train in stage I gradually arrived at a steady state. Figure 14 presents the normalized HRR contour at the end of stage II. It could be seen the flow separation kept existence ahead of the injector on the $z/W = 3/8$ surface. The constant origin of the subsonic region at $x = 0.22$ mm in Figs. 12 and 14 indicated the shock reflection locations changed little, which was consistent with the gradually stabilized pressure-rise origin in Fig. 7. Additionally, Fig. 14 displays a little different HRR distribution from Fig. 12, which was the balance result of the flame shock interaction.

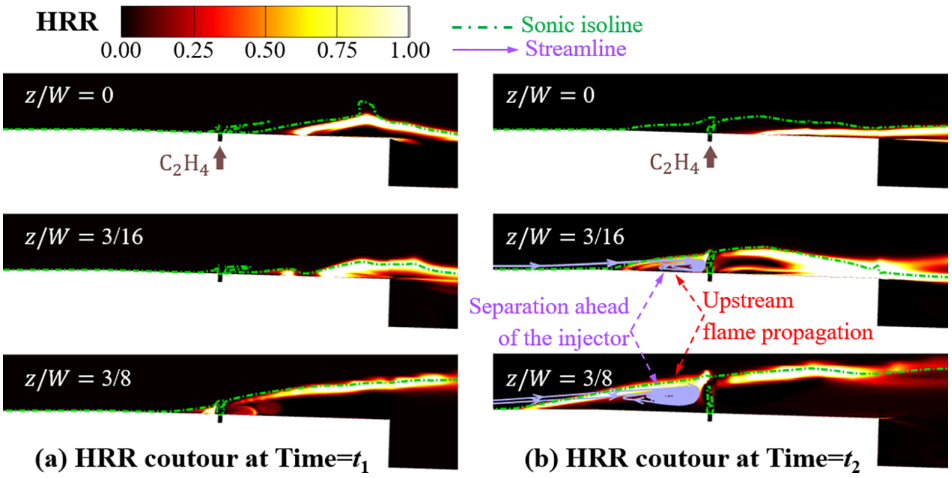

FIG. 11. The normalized HRR contours at time = t_1 and t_2, respectively, in stage I.

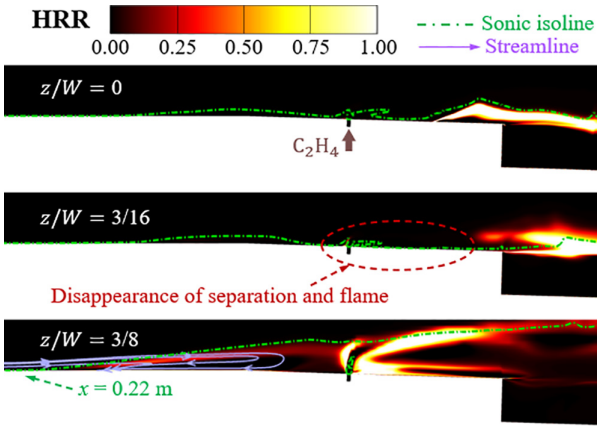

FIG. 12. The normalized HRR Contour at the end of stage I, time = t_3.

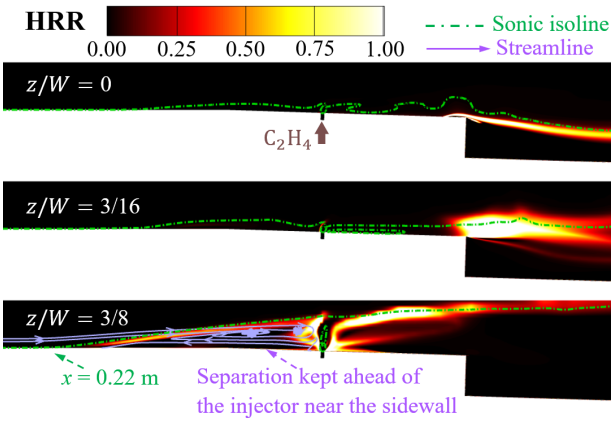

FIG. 14. The normalized HRR contour at the end of stage II, time = t_4.

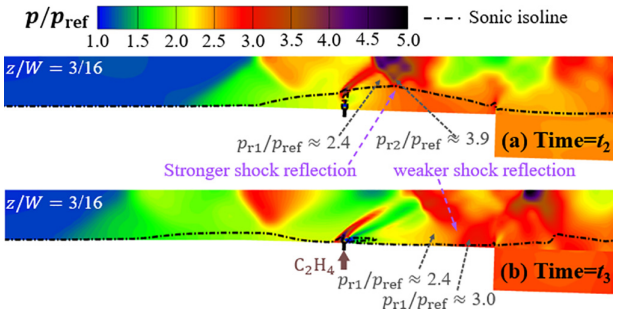

FIG. 13. Contours of normalized pressure p/p_{ref} at time = t_2 and t_3, respectively.

Stage III was a stage with changeless flame and flow inferring from Fig. 7. Figure 15 presents the normalized HRR contour on the representative $z/W = 3/16$ surface at the start and end of this stage. This chart displays that a small amount of flame occurred near the injector with a slightly enlarged subsonic region. The reason for this slight change will be discussed as follows.

Figure 16 presents the comparison of temperature contours corresponding to Fig. 15. It displays that slight temperature increases in the region downstream of the injector. Specifically, Fig. 17 plots the time-history curves of temperature T_R and stagnation temperature T_R^* at a typical point "R" in this region. It could be seen that T_R gradually increased from about 944 to 1000 K and then underwent an accelerated increase to 1146 K. The synchronous increases of T_R^* and T_R indicated the changeless flow kinetic energy. Referring to Fig. 10, the ignition delay time τ_{ign} at 900 and 1100 K was about 1.1–2.5 ms and 100–222 μs, respectively. The comparison of τ_{ign} with the previously estimated residence time $\tau_{res\text{-}m} = 131$ μs indicated that the temperature increase made auto-ignition upstream of the cavity possible, contributing to the slight flame occurrence as shown in Fig. 15. The flame occurrence could in return benefit temperature increase, showing as the accelerated increase in T_R in Fig. 17, which would further promote flame propagation.

The reason for the gradual increase in stagnation temperature is speculated as follows. According to the energy conservation equation, the increase was because the heat addition causes, including heat transfer and combustion heat release, were larger than the heat

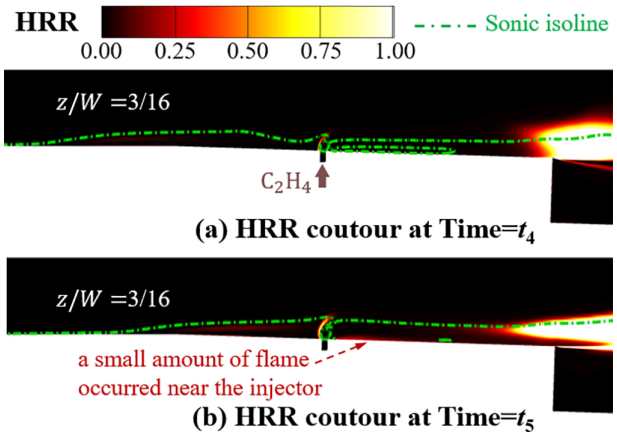

FIG. 15. The normalized HRR contours on $z/W = 3/16$ at the (a) start and (b) end of stage III, respectively.

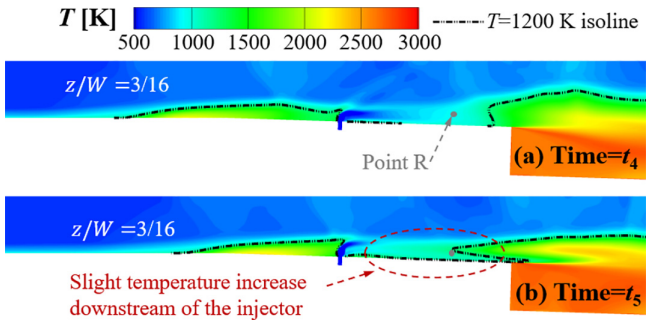

FIG. 16. Temperature contours on $z/W = 3/16$ at the (a) start and (b) end of stage III, respectively.

reduction causes, including the outflows of total enthalpy. Considering the changeless combustion flow with obvious spanwise differences in stage III, the heat-changing causes could be regarded as balanced except for the spanwise heat conduction. Namely, the spanwise heat conduction was considered as the main driving reason for the gradual

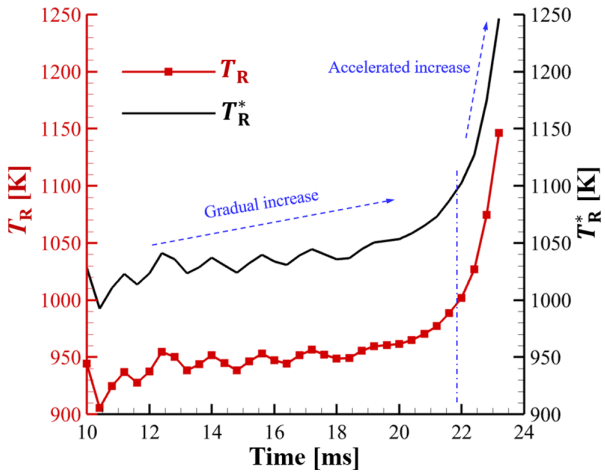

FIG. 17. Time-history curves of temperature T_R and stagination temperature T_R^* at point R from time $= t_4$ to t_5, respectively.

temperature increase. Figure 18(a) presents the schematic diagram of a simplified spanwise heat conduction model in line with the temperature contours during stage III such as Fig. 18(b). According to Fig. 18(a), the energy equation of the low-temperature region is simplified as below:

$$\lambda \cdot \frac{T_H - T_L}{\Delta z_1} \cdot A_z \cdot \tau_{HC} = c_p \cdot \rho \cdot A_z \cdot \Delta z_2 \cdot \Delta T. \quad (2)$$

All the variables were treated as constant values. λ of about 0.11 W/(m K) was the thermal conductivity. T_H and T_L of about 2500 and 950 K were the averaged temperatures of the high-temperature and low-temperature regions, respectively. Δz_1 of about 0.015 m was the spanwise distance between the two regions. A_z was the spanwise cross-sectional area. τ_{HC} was the characteristic time of the gradual stagnation temperature increase. c_p of about 1500 J/(kg K) was the constant-pressure specific heat. ρ of about 0.5 kg/m^3 was the density. Δz_2 of about 0.002 m was the approximate width of the low-temperature region separated by the threshold value of 1150 K. ΔT of about 100 K was the gradual increase in stagnation temperature

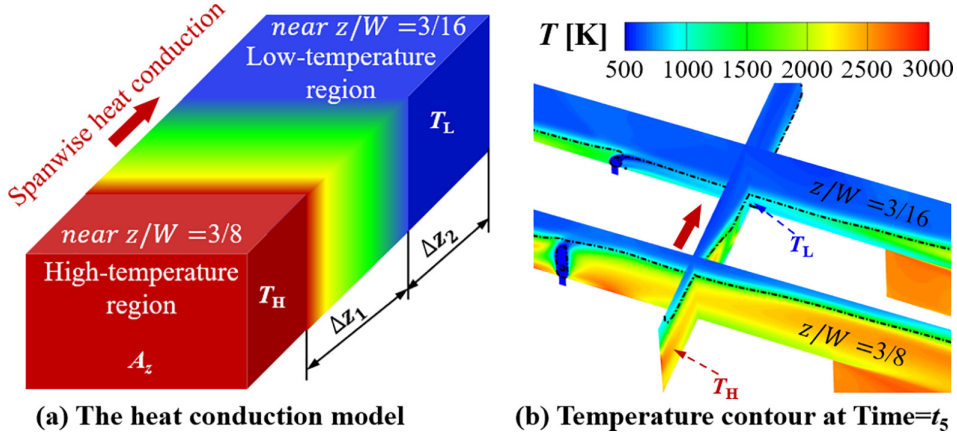

FIG. 18. Schematic diagram of a simplified spanwise heat conduction model.

referring to Fig. 17. By Eq. (2), τ_{HC} was estimated to be about 13.2 ms, close to the sustaining time of stage III. This in return testified that the reason speculation of the temperature increase was reasonable.

Stage IV was a stage with a rapid downstream flame recession, which was the reverse process of the upstream flame flashback in stage I. Figure 19 presents the normalized HRR contours at the start and middle of stage IV. It could be seen that the flame propagated upstream of the cavity on the $z/W = 3/16$ surface. This was attributed to the subsequent development after the gradual temperature increase illustrated in Figs. 16–18. Meanwhile, the downstream recession of the flame front contrastively occurred on the $z/W = 3/8$ surface along with the smaller separation ahead of the injector. The reason is discussed as follows.

Figure 20 presents the comparison of pressure contours corresponding to Fig. 19. This chart shows that the pressure-rise p_s/p_{ref} of the initial shock kept constant at 1.8, fitting with the free interaction theory of the shock/boundary layer.[44] However, the combustion-zone pressures decreased. Specifically, the pressure-rise p_b/p_{ref} ahead of the cavity decreased from 2.4 to 2.1. This was attributed to the enhanced flame mostly in the subsonic region as shown in Fig. 19(b). Because according to 1D flow equations, heat release in the subsonic flow would result in pressure decrease. The back-pressure decrease consequently generated the smaller separation in Fig. 19(b). The smaller separation was adverse for mixing and combustion, and thus, the flame ahead of the injector would further recede downstream until reaching the state at the start of stage I as shown in Fig. 11(a). Then, the next cycle of the above four stages would repeatedly continue.

C. Flame propagation analyses

The above sections have analyzed the characteristics of the periodic flame flashback process and explained its mechanism from the view of flame flow structural evolutions. This section will further elucidate the inherent mechanism of flame propagation during this process.

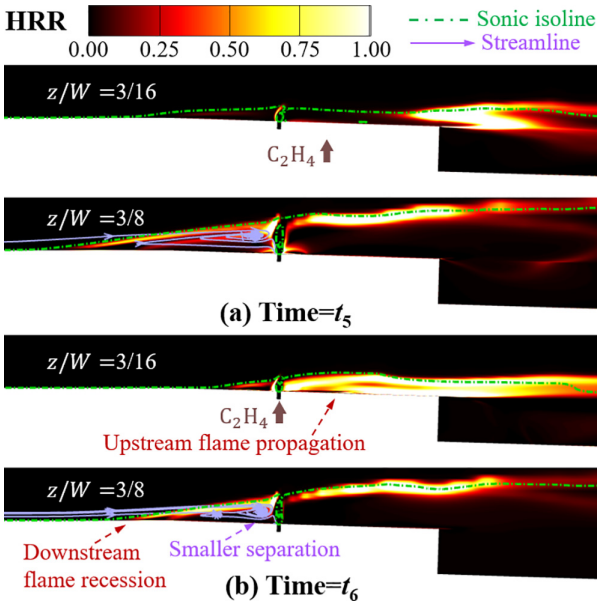

FIG. 19. HRR contours at the (a) start and (b) middle of stage IV, respectively.

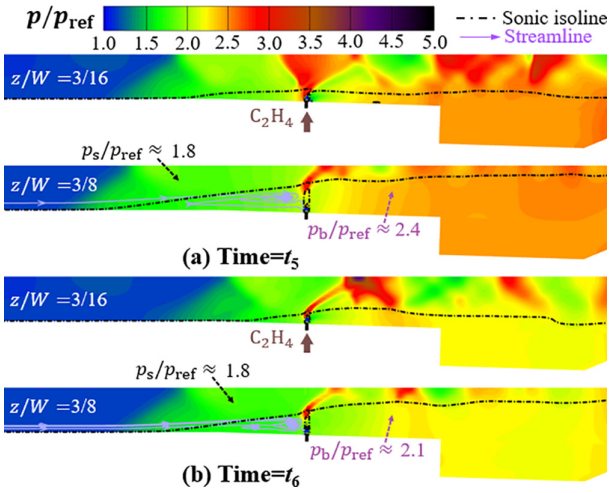

FIG. 20. Comparison of pressure contours at the (a) start and (b) middle of stage IV, respectively.

As illustrated in Sec. III B, the HRR distributions on the $z/W = 3/8$ surface were representative of the actual 3D flame structures. Figure 21 presents the schematic diagram of a simplified flame-spreading model to describe the flame propagation on this surface. The geometric expansion was ignored. u_F was the flame propagation speed along the normal direction of the flame front. u_x was the flow velocity in direction x, ignoring the flow velocities in other directions. u_{xn} was the component of u_x normal to the flame front. θ was the flame spreading angle, namely, the intersection angle of the flame front and the inflow direction x. L_{RF} was the moving distance of the flame front in direction x during the period of $\Delta\tau$. u_{RF} was the flame speed relative to the combustor wall. Referring to Fig. 21, the following equations could be achieved:

$$\begin{aligned} u_{xn} &= u_x \cdot \sin\theta, \\ L_{RF} &= -(u_F - u_{xn}) \cdot \Delta\tau / \sin\theta, \\ u_{RF} &= \frac{L_{RF}}{\Delta\tau}. \end{aligned} \tag{3}$$

Then, the below equation could be deduced:

$$u_F = (u_x - u_{RF}) \cdot \sin\theta. \tag{4}$$

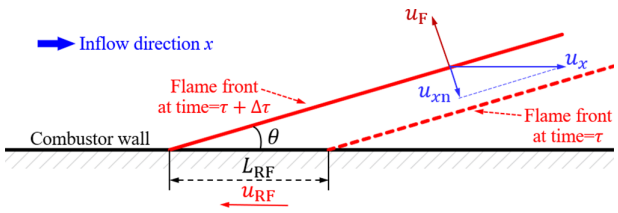

FIG. 21. Schematic diagram of the simplified flame spreading model.

On the $z/W = 3/8$ surface, the flame spreading angle θ, the flow velocity u_x near the flame front leading point, and the moving distance L_{RF-s} of the leading point during one time step size $\Delta\tau_s$ could be directly achieved from the numerical data. The relative flame speed u_{RF} could be obtained as $u_{RF} = L_{RF\text{-}s}/\Delta\tau_s$. Then, the flame propagation speed u_F could be obtained via Eq. (4). Figure 22 plots the resulting time-history curves of u_x, θ, u_F, and u_{RF} on the $z/W = 3/8$ surface. It can be seen that the relative flame speed u_{RF} was less than 80 m/s. Meanwhile, the flame propagation speed u_F of around 80–160 m/s was much smaller than the flow speed u_x of 400–750 m/s. The u_F can be further compared with theoretically estimated flame speeds to elucidate the flame propagation mechanism as follows.

The estimation methods of theoretical flame speeds are introduced below. A typical initial condition of the pressure of 176 kPa and the temperature of 700 K was chosen referring to flow parameters upstream of the flame fronts. Under this condition, the laminar flame speed u_L was calculated by the Cantera software[45] using the 1D freely propagating premixed flame model with the aforementioned two-step kinetics. The turbulent flame speed u_T was obtained by the following empirical equation:[46]

$$u_T = 4.3\frac{u'}{\sqrt{\ln\left(1+\frac{u'}{u_L}\right)}}, \tag{5}$$

u' was the turbulent velocity fluctuation calculated as $u' = \sqrt{2k_T/3}$, where k_T was turbulent kinetic energy. For simplicity, u' was treated as constantly 100 m/s, the typical value in the combustion region. Except for the turbulent flame, detonation, and deflagration waves were also possible flame propagation mechanisms. The C–J detonation speed $u_{detonation}$ was calculated by the NASA CEA program.[47] Then, the C–J deflagration speed $u_{deflagration}$ was evaluated as below:[24]

$$u_{deflagration} = \frac{\gamma(\gamma-1)+2(\gamma+1)}{2(\gamma+1)^2}\cdot u_{detonation}, \tag{6}$$

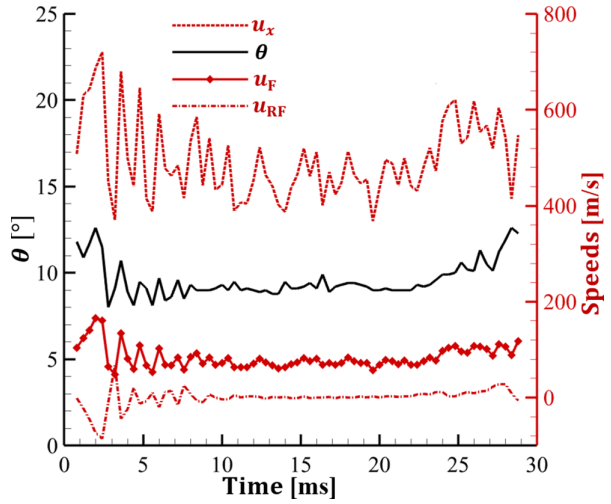

FIG. 22. Time-history curves of θ, u_x, u_F, and u_{RF} on the $z/W = 3/8$ surface.

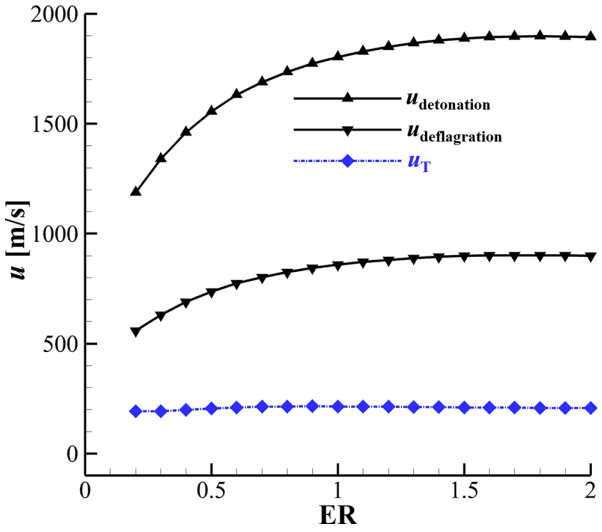

FIG. 23. Theoretical flame propagation speeds, including turbulent flame speed u_T, C–J detonation speed $u_{detonation}$, and C–J deflagration speed $u_{deflagration}$.

where γ was the specific heat ratio. By the above-mentioned methods, Fig. 23 plots the theoretical flame speeds u_T, $u_{detonation}$, and $u_{deflagration}$ at different ER conditions. It could be seen that the u_T around 200 m/s was close to the u_F of around 80–160 m/s as shown in Fig. 22. Meanwhile, the $u_{detonation}$ and $u_{deflagration}$ were much larger than u_F. Consequently, the current flame dynamics were dominated by the turbulent flame propagations, rather than the C–J detonation or deflagration speculated in previous studies.[23,24,32]

IV. CONCLUSION

This paper numerically studied the periodic flame flashback phenomenon in a cavity-based ethylene-fueled scramjet combustor. The air inflow Mach number, stagnation temperature, and stagnation pressure were 2.6, 1225 K, and 1836 kPa, respectively. The fuel was injected upstream of the cavity with a total ER of 0.29. A 3D URANS solver with a recognized two-step kinetic model was adopted for simulation. Results presented a low-frequency oscillation process with sizable flame-front movements and large-amplitude variations of wall-pressures and thrust in a fundamental period of about 27 ms. The overall features were illustrated in detail. The evolution mechanism of this process was explained by analyses of flame flow structures, and the flame propagation mechanism was recognized. The main conclusions are summarized as follows:

1. Spectral analyses of pressure and thrust data proved that the process was not driven by thermo-acoustic instabilities. Moreover, 1D wall-pressure distributions manifested the combustion kept in the separated scramjet mode accompanied by the periodic establishment and vanishment of flow separation near the injector. This differed from previous studies of flame flashbacks associated with the ramjet/scramjet combustion mode transitions.[22–29]
2. A mechanism with four evolution stages (stages I–IV) was proposed to elucidate the flow–flame interaction. In stage I, there was plentiful well-mixed unburned gas with an auto-ignition tendency due to high temperatures in the near-sidewall

low-speed region. This contributed to the rapid flame flashback upstream and shock-train extension. In stage II, the combustion-induced back-pressure and the shock-train gradually achieved an aerodynamic balance. In stage III, the combustion flow was changeless, while temperature gradually increased upstream of the cavity in the region away from the sidewall. A simplified heat conduction model was proposed to explain the temperature increase as a result of the spanwise heat conduction. The increased temperature would trigger upstream flame propagation with enhanced heat release due to auto-ignition. Nevertheless, the enhanced heat release was mostly in the subsonic flow, resulting in pressure decreases according to 1D flow equations. The decreased back-pressures generated a smaller near-sidewall separation, thus inducing a rapid flame recession downstream in stage IV.

3. A simplified flame-spreading model was proposed to illuminate the flame propagation mechanism. The comparison of flame propagation speeds by this model with theoretical estimations indicated that the current flame dynamics were dominated by turbulent flame propagations, rather than the C–J detonation or deflagration in previous studies.[23,24,32]

The current study provides updated insight into the flame flashback phenomenon in a scramjet combustor. The conclusions are suitable for the popular combustor configuration of fuel injection upstream of the cavities. They are expected to be helpful for the design and control of scramjet combustors. Further study should be done to provide methods for suppressing this phenomenon to produce smooth thrusts.

ACKNOWLEDGMENTS

This work was supported by the National Natural Science Foundation of China (Grant Nos. U2141220 and 11672309).

AUTHOR DECLARATIONS

Conflict of Interest

The authors have no conflicts to disclose.

Author Contributions

Shengzu Guo: Writing – original draft (equal). **Xu Zhang:** Writing – review & editing (equal). **Qili Liu:** Investigation (equal). **Lianjie Yue:** Formal analysis (supporting).

DATA AVAILABILITY

The data that support the findings of this study are available within the article.

REFERENCES

[1]J. Urzay, "Supersonic combustion in air-breathing propulsion systems for hypersonic flight," Annu. Rev. Fluid Mech. **50**, 593–627 (2018).
[2]Y. Tian, S. H. Yang, J. L. Le, F. Y. Zhong, and X. Q. Tian, "Investigation of combustion process of a kerosene fueled combustor with air throttling," Combust. Flame **179**, 74–85 (2017).
[3]Y. Tian, J. L. Le, S. H. Yang, and F. Y. Zhong, "Investigation of combustion characteristics in a kerosene-fueled supersonic combustor with air throttling," AIAA J. **58**(12), 5379–5388 (2020).
[4]W. Bao, J. C. Hu, Y. H. Zong, Q. C. Yang, J. T. Chang, M. Wu, and D. R. Yu, "Ignition characteristics of a liquid-kerosene-fueled scramjet during air throttling combined with a gas generator," J. Aerosp. Eng. **27**(5), 06014003–06014006 (2014).
[5]B. X. Wei, X. Xu, M. L. Yan, X. X. Shi, and Y. Yang, "Study on aeroramp injector/gas-pilot flame in a supersonic combustor," J. Propul. Power **28**(3), 486–495 (2012).
[6]B. Chen, X. Xu, B. X. Wei, and Y. Zhang, "Numerical simulations of turbulent flows in aeroramp injector/gas-pilot flame scramjet," Chin. J. Aeronaut. **30**(4), 1373–1390 (2017).
[7]R. D. Rockwell, C. P. Goyne, W. Haw, R. H. Krauss, J. C. McDaniel, and C. J. Trefny, "Experimental study of test-medium vitiation effects on dual-mode scramjet performance," J. Propul. Power **27**(5), 1135–1142 (2011).
[8]Z. G. Wang, H. B. Wang, and M. B. Sun, "Review of cavity-stabilized combustion for scramjet applications," Proc. Inst. Mech. Eng., Part G **228**(14), 2718–2735 (2014).
[9]A. Oamjee and R. Sadanandan, "Effects of fuel injection angle on mixing performance of scramjet pylon-cavity flameholder," Phys. Fluids **32**(11), 116108 (2020).
[10]W. Shi, Y. Tian, J. L. Le, and F. Y. Zhong, "Effect of pilot hydrogen on the formation of dynamic flame in an ethylene-fueled scramjet with a cavity," Phys. Fluids **33**(5), 055130 (2021).
[11]Y. Tian, W. Shi, F. Y. Zhong, and J. L. Le, "Pilot hydrogen enhanced combustion in an ethylene-fueled scramjet combustor at Mach 4," Phys. Fluids **33**(1), 015105 (2021).
[12]Y. Tian, M. M. Guo, W. Ran, J. L. Le, and F. Y. Zhong, "Experimental investigation of effects of pulsed injection on flow structure and flame development in a kerosene-fueled scramjet with pilot hydrogen," Phys. Fluids **34**(5), 055109 (2022).
[13]B. An, Z. G. Wang, and M. B. Sun, "Flame stabilization enhancement by microjet-based virtual shock wave generators in a supersonic combustor," Phys. Fluids **33**(1), 016104 (2021).
[14]T. Hiejima and T. Oda, "Shockwave effects on supersonic combustion using hypermixer struts," Phys. Fluids **32**(1), 016104 (2020).
[15]J. T. Chang, J. L. Zhang, W. Bao, and D. R. Yu, "Research progress on strut-equipped supersonic combustors for scramjet application," Prog. Aeronaut. Sci. **103**, 1–30 (2018).
[16]Q. L. Liu, D. Baccarella, and T. H. Lee, "Review of combustion stabilization for hypersonic airbreathing propulsion," Prog. Aeronaut. Sci. **119**, 100636 (2020).
[17]K. C. Lin, K. Jackson, R. Behdadnia, T. A. Jackson, F. H. Ma, and V. Yang, "Acoustic characterization of an ethylene-fueled scramjet combustor with a cavity flameholder," J. Propul. Power **26**(6), 1161–1170 (2010).
[18]H. B. Wang, M. B. Sun, N. Qin, H. Y. Wu, and Z. G. Wang, "Characteristics of oscillations in supersonic open cavity flows," Flow, Turbul. Combust. **90**(1), 121–142 (2013).
[19]M. Kumar and A. Vaidyanathan, "Oscillatory mode transition for supersonic open cavity flows," Phys. Fluids **30**(2), 026101 (2018).
[20]X. Zhang, L. J. Yue, T. L. Huang, Q. F. Zhang, and X. Y. Zhang, "Numerical investigation of mode transition and hysteresis in a cavity-based dual-mode scramjet combustor," Aerosp. Sci. Technol. **94**, 105420 (2019).
[21]D. J. Micka and J. F. Driscoll, "Combustion characteristics of a dual-mode scramjet combustor with cavity flameholder," Proc. Combust. Inst. **32**(2), 2397–2404 (2009).
[22]M. L. Fotia and J. F. Driscoll, "Ram-scram transition and flame/shock-train interactions in a model scramjet experiment," J. Propul. Power **29**(1), 261–273 (2013).
[23]Z. G. Wang, M. B. Sun, H. B. Wang, J. F. Yu, J. H. Liang, and F. C. Zhuang, "Mixing-related low frequency oscillation of combustion in an ethylene-fueled supersonic combustor," Proc. Combust. Inst. **35**(2), 2137–2144 (2015).
[24]M. B. Sun, X. D. Cui, H. B. Wang, and V. Bychkov, "Flame flashback in a supersonic combustor fueled by ethylene with cavity flameholder," J. Propul. Power **31**(3), 976–981 (2015).
[25]H. Ouyang, W. D. Liu, and M. B. Sun, "The influence of cavity parameters on the combustion oscillation in a single-side expansion scramjet combustor," Acta Astronaut. **137**, 52–59 (2017).
[26]G. Y. Zhao, M. B. Sun, Y. N. Wang, X. P. Li, and H. B. Wang, "Investigations of injection parameters on combustion oscillation in a supersonic crossflow," Acta Astronaut. **152**, 426–436 (2018).

[27]G. Y. Zhao, M. B. Sun, X. L. Song, X. P. Li, and H. B. Wang, "Experimental investigations of cavity parameters leading to combustion oscillation in a supersonic crossflow," Acta Astronaut. **155**, 255–263 (2019).
[28]G. Y. Zhao, M. B. Sun, J. S. Wu, X. D. Cui, and H. B. Wang, "Investigation of flame flashback phenomenon in a supersonic crossflow with ethylene injection upstream of cavity flameholder," Aerosp. Sci. Technol. **87**, 190–206 (2019).
[29]G. Y. Zhao, J. H. Du, M. J. Liu, H. B. Wang, and M. B. Sun, "Numerical investigation of the scale effects of the flame flashback phenomenon in scramjet combustors," Aerosp. Sci. Technol. **119**, 107165 (2021).
[30]D. G. Cao, H. E. Brod, N. Yokev, and D. Michaels, "Flame stabilization and local combustion modes in a cavity-based scramjet using different fuel injection schemes," Combust. Flame **233**, 111562 (2021).
[31]S. H. Zhu and X. Xu, "Experimental study on flame transition in a two-stage struts dual-mode scramjet," J. Aerosp. Eng. **30**(5), 06017002 (2017).
[32]S. H. Zhu, X. Xu, Q. C. Yang, and Y. S. Jin, "Intermittent back-flash phenomenon of supersonic combustion in the staged-strut scramjet engine," Aerosp. Sci. Technol. **79**, 70–74 (2018).
[33]J. L. Zhang, J. T. Chang, Z. A. Wang, L. Gao, and W. Bao, "Flame propagation and flashback characteristics in a kerosene fueled supersonic combustor equipped with strut/wall combined fuel injectors," Aerosp. Sci. Technol. **93**, 105303 (2019).
[34]W. H. Heiser and D. T. Pratt, in *Hypersonic Airbreathing Propulsion*, AIAA Education Series (AIAA, 1994).
[35]X. Zhang, Z. J. Wu, L. J. Yue, Z. B. Gao, W. H. Luo, and H. Chen, "Fuel regulation historical effects on flame stabilizations in a cavity-based scramjet combustor," AIAA J. **60**(4), 2694–2700 (2022).
[36]X. Zhang, Q. F. Zhang, Z. J. Wu, L. J. Yue, Z. B. Gao, W. H. Luo, and H. Chen, "Experimental study of hysteresis and catastrophe in a cavity-based scramjet combustor," Chin. J. Aeronaut. **35**(10), 118–133 (2022).
[37]H. B. Wang, Z. G. Wang, M. B. Sun, and H. Y. Wu, "Combustion modes of hydrogen jet combustion in a cavity-based supersonic combustor," Int. J. Hydrogen Energy **38**(27), 12078–12089 (2013).
[38]F. R. Menter, "Two-equation eddy-viscosity turbulence models for engineering applications," AIAA J. **32**(8), 1598–1605 (1994).
[39]C. K. Westbrook and F. L. Dryer, "Simplified reaction mechanisms for the oxidation of hydrocarbon fuels in flames," Combust. Sci. Technol. **27**, 31–43 (1981).
[40]L. W. Cheng, F. Q. Zhong, Z. P. Wang, H. B. Gu, S. G. Ma, and X. Y. Zhang, "Experimental study of ignition and flame characteristics of surrogate of cracked hydrocarbon fuels in supersonic crossflow," AIAA Paper No. 2017-2295, 2017.
[41]X. Zhang, "Combustion flow characteristics of supersonic combustion mode transitions and hysteresis," Ph. D. dissertation (University of Chinese Academy of Sciences, 2020) (in Chinese).
[42]F. H. Ma, J. Li, V. Yang, K. C. Lin, and T. A. Jackson, "Thermoacoustic flow instability in a scramjet combustor," AIAA Paper No. 2005-3824, 2005.
[43]X. Xiang and H. Babinsky, "Corner effects for oblique shock wave/turbulent boundary layer interactions in rectangular channels," J. Fluid Mech. **862**, 1060–1083 (2019).
[44]D. R. Chapman, D. M. Kuehn, and H. K. Larson, "Investigation of separated flows in supersonic and subsonic streams with emphasis on the effect of transition," Report No. NACA-TR-1356, 1958.
[45]D. G. Goodwin, H. K. Moffat, I. Schoegl, R. L. Speth, and B. W. Weber (2022). "Cantera: An object-oriented software toolkit for chemical kinetics, thermodynamics, and transport processes," Zenodo, Version 2.6.0.https://www.cantera.org
[46]Q. Zhang and X. Q. Huang, *Aeroengine Combustion* (National Defense Industry Press, 2015) (in Chinese).
[47]S. Gordon and B. J. McBride, *Computer Program for Calculation of Complex Chemical Equilibrium Compositions and Applications* (NASA Lewis Research Center, 1996).